On Electromagnetic Modulation of Flow Instabilities, Mixing and Heat Transfer in Conducting and Magnetized Fluids

Kenjeres, S.

DOI
10.1088/1742-6596/745/2/022003

Publication date
2016

Document Version
Final published version

Published in
Journal of Physics: Conference Series

On Electromagnetic Modulation of Flow Instabilities, Mixing and Heat Transfer in Conducting and Magnetized Fluids

On Electromagnetic Modulation of Flow Instabilities, Mixing and Heat Transfer in Conducting and Magnetized Fluids

S Kenjeres[1]
Transport Phenomena Section, Department of Chemical Engineering, Faculty of Applied Sciences and J. M. Burgerscentrum for Fluid Mechanics, Delft University of Technology, The Netherlands

E-mail: s.kenjeres@tudelft.nl

Abstract. In the present paper we give a concise review of some recent highlights of our research dealing with electromagnetic control of flow, mixing and heat transfer of electrically conductive or magnetized fluids. We apply a combination of state-of-art numerical (DNS and LES) and experimental (PIV and LIF) techniques to provide fundamental insights into the complex phenomena of interactions between imposed (or induced) electromagnetic fields and underlying fluid flow. Our analysis covers an extensive range of working fluids, i.e. weakly- and highly-electrically-conductive, as well as magnetized fluids. These interactions are defined through the presence of different types of body forces acting per volume of fluid. A fully closed system of governing equations containing an extended set of the Navier-Stokes and a simplified set of the Maxwell equations is presented. The four characteristic examples are selected: the electromagnetic control of self-sustained jet oscillations, the electromagnetic enhancement of heat transfer in thermal convection, the wake interactions behind magnetic obstacles and finally, the thermo-magnetic convection in differentially heated cubical enclosure. The comparative assessment between experimental and numerical results is presented. It is concluded that generally good agreement between simulations and experiments is obtained for all cases considered, proving the concept of electromagnetic modulation, which can be used in numerous technological applications.

1. Introduction

Examples of flow of electrically conductive or magnetized fluids include numerous situations in astrophysical, geophysical, environmental and technological applications, [1], [2], [3]. In the present review, we focus primarily on technological and industrial applications where the imposed electro-magnetic fields can significantly affect the underlying flow, mixing and heat transfer, but there is no back-reaction on the initially imposed magnetic field (i.e. we consider the one-way interactions, [4]). In the first part, we focus on weakly and strongly electrically conductive fluids. For the weakly conductive fluids, it is necessary to impose a combination of external magnetic and electric fields, [5], [6], [7]. This is done in order to be able to generate sufficiently strong Lorentz force. Here, suitable orientations between imposed multiple magnetic and electric flux lines result in specific spatial distribution of the Lorentz force that imposes vortical flow structures (dwarf tornados), [5]-[12]. This feature can be very beneficial in disturbing the hydrodynamical and thermal boundary layers along solid boundaries. In the case of strongly conductive fluids, only external magnetic fields need to be

[1] To whom any correspondence should be addressed.

imposed since the induced electric current is sufficient to produce a significant Lorentz force, [4], [13]. In the second part, we address non-conductive magnetized fluids. For such fluids, there is no electric current generated, [14-17]. Here it is necessary to apply quite strong magnetic field induction gradients (due to relatively low value of the magnetic susceptibility of the paramagnetic and diamagnetic fluids) to be able to produce sufficiently strong magnetization (Kelvin) forces, [18-22]. The primary goal of our investigation is to be able to provide fundamental insights into the complex mechanism of electromagnetic field interactions with electrically conductive and magnetized fluids. The major challenge is in the fact that we need to provide simultaneously instantaneous distributions of the velocity, temperature (or concentration) and of the electric current and its potential. The typical electrically conductive liquid (liquid metals) is also non-transparent. Moreover, we need to address situations in which a coexistence of different flow regimes (laminar, transitional, fully turbulent) is present within a single domain. All this results in conditions that are notoriously difficult for standard experimental techniques. Our research strategy lies in developing the integrated numerical simulation approaches, which are able to cover an extensive range of working parameters. Here, the integrated approach defines a single computational algorithm able to solve both Navier-Stokes and Maxwell's equations. In parallel with the numerical simulations, we design and build suitable experimental setups, where some of the advanced measuring techniques still can be applied. The experimental datasets obtained are then used to validate the results of numerical simulations. In this paper, we present a short overview of some of our most recent work that is based on such a combined experimental/numerical simulations approach.

2. Mathematical description of the electromagnetic/fluid flow/heat transfer interactions

In this section we give a short overview of the transport equations required to describe the interactions between imposed (or induced) electromagnetic fields and the flow of conductive or magnetized fluids. The system of equations consists of conservation of the momentum and energy together with the divergence free conditions for the velocity (**v**), magnetic field (**b**) and total electric current (**j**). We start with the conservation of momentum equations, where different body forces acting per fluid element volume are added as:

$$\frac{\partial \mathbf{v}}{\partial t}+(\mathbf{v}\cdot\nabla)\mathbf{v}=-\frac{1}{\rho}\nabla p+\nu\nabla^2\mathbf{v}+\mathbf{f}^{\mathrm{b}}+\mathbf{f}^{\mathrm{l}}+\mathbf{f}^{\mathrm{m}} \tag{1}$$

where 'ρ' is the fluid density and 'ν' is the kinematic viscosity. The additional body forces on the right-hand-side of the momentum equation represent the thermal buoyancy ($\mathbf{f}^{\mathrm{b}}$), Lorentz force ($\mathbf{f}^{\mathrm{l}}$) and magnetization force ($\mathbf{f}^{\mathrm{m}}$), respectively, which are calculated as:

$$\mathbf{f}^{\mathrm{b}}=-\beta\mathbf{g}(\theta-\theta_0),\ \mathbf{f}^{\mathrm{l}}=\frac{1}{\rho}(\mathbf{j}\times\mathbf{b}),\ \mathbf{f}^{\mathrm{m}}=\frac{\chi}{2\mu_0}\nabla\mathbf{b}^2 \tag{2}$$

where 'β' is the thermal expansion coefficient, 'θ_0' is the reference temperature, 'χ' is the magnetic susceptibility and 'μ_0' is the magnetic constant. For the thermal buoyancy term ($\mathbf{f}^{\mathrm{b}}$), an additional transport equation for temperature is solved:

$$\frac{\partial \theta}{\partial t}+(\mathbf{v}\cdot\nabla)\theta=a\nabla^2\theta \tag{3}$$

where the thermal diffusivity is $a=\nu/\mathrm{Pr}$. The Lorentz force term requires ($\mathbf{f}^{\mathrm{l}}$) information about the imposed magnetic field (**b**) and of the total current density (**j**). The total electric current density (**j**), under the assumption that the induced magnetic field is much weaker than its imposed counterpart (which is valid for $\mathrm{Re_M}= v_0 D/\lambda \ll 1$, where ($\lambda$) is magnetic diffusivity – or so called one-way interactions between fluid flow and electromagnetic fields, [23]) is calculated from the Ohm's law for a moving conductive medium that can be written as:

$$\mathbf{j} = \sigma\left(-\nabla\phi + \mathbf{v}\times\mathbf{b}\right) \tag{4}$$

where 'σ' is the electric conductivity of fluid. By imposing the divergence-free condition, the final equation for electric potential is obtained as:

$$\nabla\cdot\mathbf{j} = 0 \rightarrow \nabla^2\phi = \nabla\cdot\left(\mathbf{v}\times\mathbf{b}\right) \tag{5}$$

The electric potential can be solved if the value of the magnetic field (**b**) is available. The most elaborate approach is to deal with a full transport equation for the magnetic field induction, which can be derived by combining different subsets of the Maxwell equations. This is a standard approach for the two-way coupled MHD problems. Since we are dealing with the one-way coupled phenomena (Re_M<<1), we apply a simpler Biot-Savart law for magnetic field as:

$$\mathbf{b} = \frac{\mu_0 i}{4\pi}\int\frac{d\mathbf{s}\times\mathbf{r}}{r^3} \tag{6}$$

where '$d\mathbf{s}$' is the length of the differential element of the current-carrying wire, 'r' is the distance from the wire and 'i' is the electric current density through the wire. For magnetized fluids, there is no electric current generated, so the only remaining body forces are due to the thermal buoyancy and magnetization. By applying the Boussinesq approximation for fluid density and magnetic susceptibility, the final form of the magnetization force can be written as:

$$\mathbf{f}^{\mathrm{m}} = -\frac{1}{\rho_0}\left(1+\frac{1}{\beta\theta_0}\right)\frac{\chi_0\beta\left(\theta-\theta_0\right)}{2\mu_0}\nabla\left|b_0\right|^2 \tag{7}$$

where 'χ_0' is the magnetic susceptibility at the reference temperature. Now, we have a fully closed system of equations (1)-(6) that can be applied for a vast range of interactions between the flow and electromagnetic forcing of electrically conductive (both weakly- and strongly-conductive) as well as magnetized fluids. It is convenient to introduce the non-dimensional forms of the constitutive equations. The following set of non-dimensional parameters is used:

- The neutral fluids:

$$\mathrm{Re} = \frac{\mathrm{V_0 D}}{\nu},\ \mathrm{Ra_T} = \frac{\beta g\Delta\theta\,\mathrm{Pr}\,\mathrm{D}^3}{\nu^2},\ \mathrm{Pr} = \frac{\nu}{a} \rightarrow \text{Reynolds, Rayleigh (thermal) and Prandtl}$$

- The electrically conductive fluids:

$$\mathrm{Re_M} = \frac{\mathrm{V_0 D}}{\lambda},\ \mathrm{N} = \frac{\sigma\,|\,\mathrm{b_0}\,|^2\,\mathrm{D}}{\rho\mathrm{V_0}},\ \mathrm{Ha} = \left(\mathrm{Re\,N}\right)^{1/2} \rightarrow \text{Reynolds (magnetic), Stuart and Hartmann}$$

- The magnetized fluids:

$$\mathrm{Ra_M} = \frac{\beta\gamma^*\Delta\theta\,\mathrm{Pr}\,\mathrm{D}^3}{\nu^2},\ \gamma = \frac{\chi_0\,|\mathrm{b_0}\,|^2}{\rho_0\mu_0 gD},\ \gamma^* = \gamma g\left[1+\left(1/\beta\theta_0\right)\right]/2 \rightarrow \text{Rayleigh (magnetic) and magnetization numbers}$$

3. Numerical and experimental methods

We have developed an in-house computer code with an integrated Navier-Stokes/Maxwell's solver for general body-fitted geometries, [8-10], [12-13], [21-25]. Here, we give just a short overview of the solver characteristic. The non-staggered numerical mesh arrangement is applied for all transport variables. The predictor-corrector type of coupling between velocity and pressure is imposed through the standard SIMPLE algorithm. The time-integration is performed by the fully implicit second-order

three-consecutive time-steps scheme. The diffusion and convection terms of the transport equations are discretized by the second-order central-differencing scheme (CDS). The three-dimensional domain-decomposition technique with message passing interface (MPI) directives is used for execution of the code on multiple processors. This makes an appropriate platform for performing the full resolving simulations, i.e. direct numerical simulations (DNS). In order to reach high values of Reynolds (Re) and Rayleigh (Ra) numbers, as well as of the interactive parameters (N), we also introduced the large-eddy simulation approach (LES). Here, we apply different subgrid scale (SGS) models. One of the possibilities is to use an extended version of the Smagorinsky type of sub-grid models for unresolved momentum and temperature equations. In this model, additional reduction of the velocity fluctuations due to the presence of the imposed magnetic field ([26]) and in the proximity of the wall ([8-10], [12]) are taken into account:

$$\tau_{ij} = \frac{1}{3}\tau_{kk} - \nu_t S_{ij}\,,\; S_{ij} = \frac{1}{2}\left(\frac{\partial \overline{u_i}}{\partial x_j} + \frac{\partial \overline{u_j}}{\partial x_i}\right),\; \nu_s = \left(C_s\Delta\right)^2\left(S_{ij}S_{ij}\right)^{1/2},$$

$$\nu_t = \nu_s exp\left[-\left(\frac{\sigma}{\rho}\right)\left(C_m\Delta\right)^2 |\,\mathrm{b}_0\,|^2 / \nu_s\right],$$

$$C_s = C_{s0}\left[1 - exp\left(\frac{-x_i^{N+}}{25}\right)\right]^2 \tag{8}$$

where ‘ $\overline{u_i}$ ‘is the resolved velocity, ‘C_{s0}’ and ‘C_m’ are the model coefficients. Similarly, the unresolved turbulent heat flux is calculated by using a simple gradient diffusion hypothesis (SGDH) model :

$$\tau_{\theta i} = -\frac{\nu_t}{\mathrm{Pr_t}}\frac{\partial \overline{\theta}}{\partial x_i} \tag{9}$$

where ‘ $\overline{\theta}$ ‘ is the resolved temperature and ‘$\mathrm{Pr_t}$’ is the turbulent Prandtl number. To account for various multi-physics phenomena such as multi-phase flows with presence of a free-surface (to simulate electromagnetic braking in continuous casting of liquid steel) or a phase-change in the presence of a strong heat source (to simulate continuous laser- of arc-welding), we develop additional modules within the OpenFOAM open-source computational toolkit, [27]. Because of its excellent computational efficiency, the in-house code is applied for all generic situations, whereas the OpenFOAM simulations are intended for the real-scale technological applications. In parallel with this development of numerical simulation codes, special attention is also devoted to application of experimental techniques. Here, we apply particle image velocimetry (PIV) and laser induced fluorescence (LIF) techniques for measurements of the velocity field and distributions of a passive scalar, [10]. For temperature and wall-heat transfer measurements, a combination of thermocouples and transparent encapsulated liquid crystals is employed [20-22]. For experiments with magnetized fluids, a specially designed superconducting magnet needs to be used [14-22]. All experimental studies with paramagnetic working fluids were performed at the Department of Fundamental Research in Energy Engineering, Faculty of Energy and Fuels, AGH University of Science and Technology in Krakow, Poland, [20-22].

4. Results and discussion

In this section, we will focus on some typical situations involving the interactions between imposed electromagnetic fields and underlying fluid flow, mixing or/and heat transfer phenomena, which we recently studied by combing experimental (PIV, LIF and thermocouple measurements) and numerical

simulation methods (DNS and LES). Here we address the following situations with the corresponding interactive forces:

- Self-sustaining jet oscillations in an isothermal turbulent flow regime ([27-30]):
  - $\mathbf{f}^{b}=0,\ \mathbf{f}^{m}=0,\ \mathbf{f}^{l}\neq 0,\ \mathbf{j}=\sigma\mathbf{e}$
- Heated-from-below thermal convection subjected to electromagnetic forcing ([8-10],[12]):
  - $\mathbf{f}^{b}\neq 0,\ \mathbf{f}^{m}=0,\ \mathbf{f}^{l}\neq 0,\ \mathbf{j}=\sigma\mathbf{e}$
- Flow and mixing behind magnetic obstacles in transitional flow regimes ([30-33]):
  - $\mathbf{f}^{b}=0,\ \mathbf{f}^{m}=0,\ \mathbf{f}^{l}\neq 0,\ \mathbf{j}=\sigma\left(-\nabla\phi+\mathbf{v}\times\mathbf{b}\right)$
- Thermo-magnetic convection of a paramagnetic fluid in a cubical enclosure ([21-22]):
  - $\mathbf{f}^{b}\neq 0,\ \mathbf{f}^{m}\neq 0,\ \mathbf{f}^{l}=0$

4.1. Electromagnetic control of self-sustaining jet oscillations

We start with the recent study in which we address different possibilities of controlling the flow of a weakly conductive fluid entering a shallow cavity, [27-30]. A physical mechanism of the self-sustained jet oscillations takes place when the incoming jet is confined in both directions perpendicular to its flow direction. This is observed for a range of Reynolds numbers, including both laminar and turbulent inlet conditions (10^2<Re<$1.7\text{x}10^5$), [34-37]. It is observed that the dimensions of the confining cavity have an important influence on the jet oscillations. The self-sustained jet oscillations disappear in very wide cavities. The physical mechanism of the self-sustaining jet oscillation is sketched in Fig.1. The generation of characteristic low-pressure and impingement regions and their mutual interactions lead to self-sustained jet oscillations. In the present work, we focus on possibilities of controlling these oscillations for electrically conductive fluids by imposed electromagnetic forcing. The setup with locations of the permanent magnets and electrodes is shown in Fig.2-left. The dimensions of the cavity filled with weakly conductive fluid are HxWxL=0.7x0.3x0.035 m^3. The working electrically conducting fluid has density $\rho = 1.1\text{x}10^3$ kg/m^3, viscosity $\nu = 1.27\text{x}10^{-6}$ m^2/s and conductivity $\sigma = 7.1$ S/m. The characteristic dimension of the square nozzle of the incoming jet is kept constant with d=0.01 m, which is submerged at d_n=0.15 m beneath the top free-surface. Two electrodes with a potential difference of $\Delta\phi = \phi_1 - \phi_2$ are placed on opposite sides of the tank at a distance L below the nozzle exit. The electrodes cover an area of 0.03x0.03 m^2. The adjustable imposed dc current (I) is either directed from left to right (I > 0) or from right to left (I < 0). Three magnets of opposite polarities are placed close to the top of the domain, in the proximity of the nozzle exit. The permanent magnets are aligned with their centers at y=-0.15 m and z=-0.045 m with a distance D=0.08 m. This combination of permanent magnets and electrodes produces a Lorentz force, the intensity and direction of which can be simply changed by regulation of the imposed electric current. We will show how this leads to selected suppression or enhancement of the jet oscillations. For this purpose, we perform combined experimental (PIV) and numerical studies (dynamic LES). The contours of the imposed magnetic field are shown in Fig.2-right/top. The characteristic profiles show an excellent agreement between measured and numerically simulated magnetic field, Fig.2-right/bottom. The time averaged vertical velocity profiles at three characteristic locations ($y = -0.18$ m, $y = -0.28$ m and $y = -0.38$ m) for Re= 4700 in the oscillation-suppressing (N = 0.017) regime for the dynamic LES (red solid line) and the PIV experiment (symbols) are shown in Fig.3. It can be seen that good agreement between simulation and experiment is obtained for all locations. Typical instantaneous velocity vectors of the self-sustained jet oscillations at different time instants are plotted in Fig.4. Here the dynamic LES results without electromagnetic forcing for incoming jet conditions at Re=4700 are selected. In addition, the method of estimating an instant jet angle (blue lines) from a least squares fit of the maximum velocity locations at fixed y (red points) is depicted. The low-pressure regions, which coincide with centers of vortical structures can be easily observed. Next, we analyze different situations by considering different values of the Reynolds number for the incoming jet as well as different orientations and intensity of the applied dc current. Distribution of the total

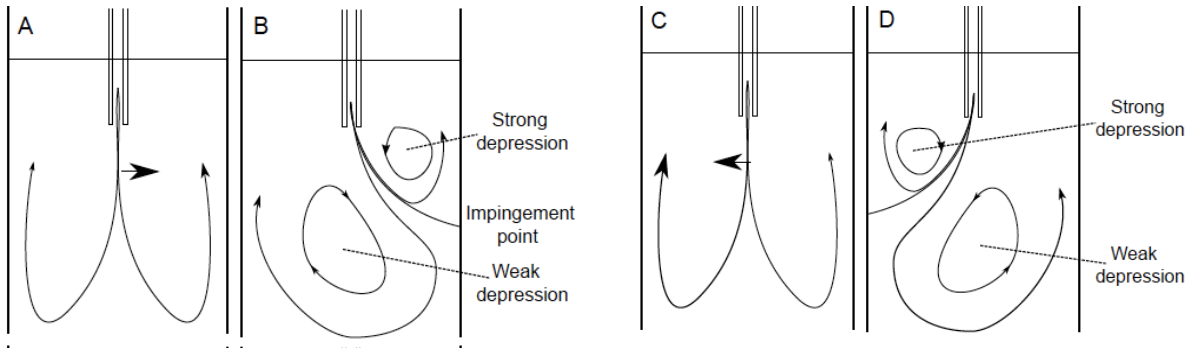

Figure 1. The physical mechanism of the self-sustaining jet oscillation (left-to-right: A&B, right-to-left: C&D) within the quasi 2D shallow enclosure with the free surface at the top, Ref.[30].

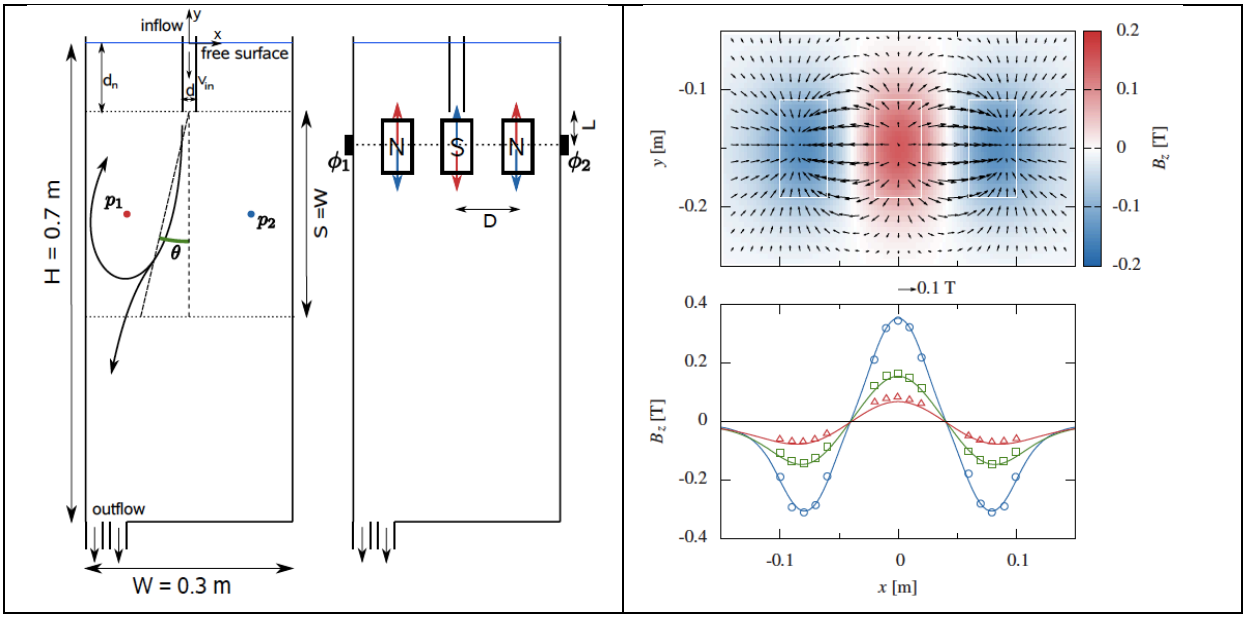

Figure 2. Geometry of the experimental/numerical setup of the self-sustaining jet oscillation with locations of the permanent magnets and electrodes (-left); Magnetic field vectors and contours of the vertical magnetic field component (B_z) (-right/top); Measured and numerically simulated profiles of the vertical magnetic field at characteristic locations (-right/bottom), Ref.[30].

energy contained in the velocity fluctuations (oscillatory/periodic + fluctuating/turbulence) is estimated from the Proper Orthogonal Decomposition (POD) modes. For this purpose, a series of PIV measurements are performed and analyzed, [29-30]. The most important results are shown in Fig.5. Here we portray energy distribution for different forcing conditions (I=0 or I=4 A) as well as for different values of Reynolds number based on the incoming jet velocity (3150<Re<7100). This is done by showing the energy contained per POD mode number (n) as a fraction of the total kinetic energy for first 30 modes. It can be seen that for lower value of Re (Re=3150), electromagnetic forcing significantly affects the distribution of the fraction of kinetic energy. For the first 4 modes contributions are suppressed, while the higher modes are slightly elevated, but approximately constant in comparison to the neutral case. For the high Re number (Re=7100), differences in distribution between passive and electromagnetic case are almost negligible, indicating the upper limit of the imposed electromagnetic forcing. A summary of the non-dimensional jet frequencies obtained (St=f

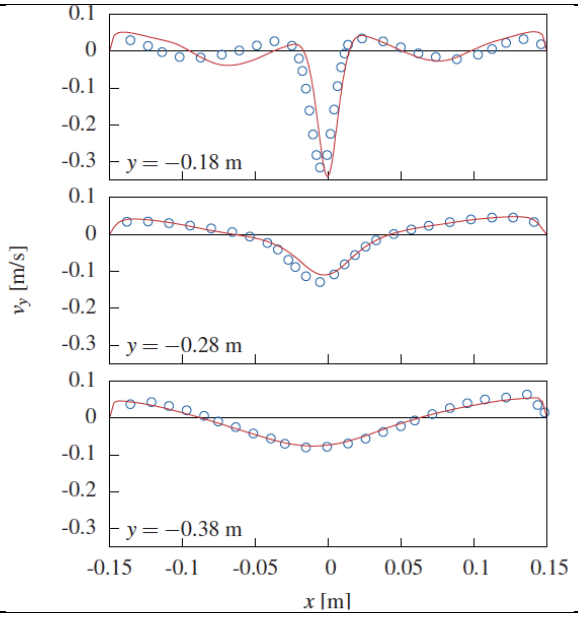

Figure 3. The time averaged vertical velocity component at three characteristic locations (y = −0.18 m, y = −0.28 m and y = −0.38 m) for Re= 4700 in the oscillation suppressing (N = 0.017) configuration for the dynamic LES (red solid line) and the PIV experiment (symbols).

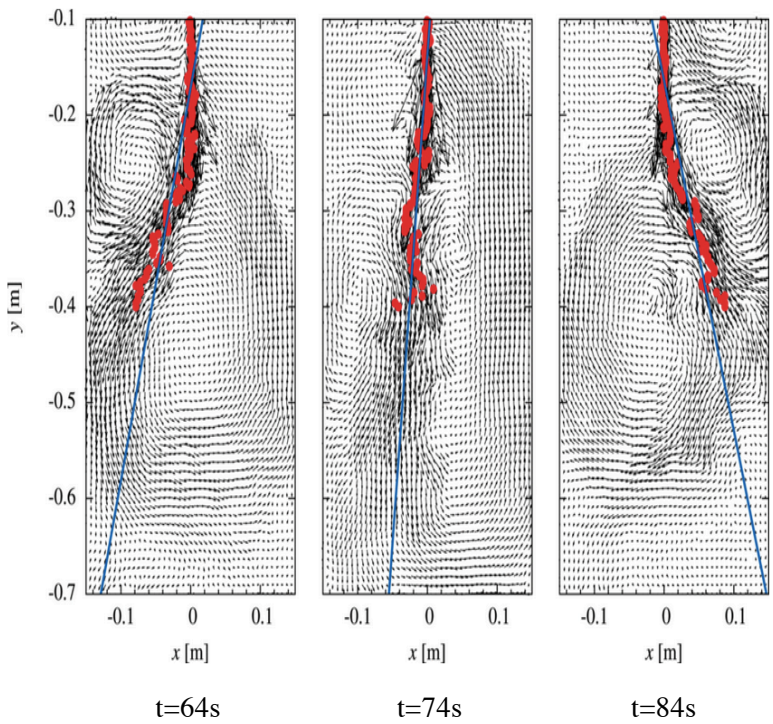

Figure 4. The instantaneous velocity field during different time instant of the self-sustained jet oscillations in a shallow cavity (t=64, 74 and 84 s – from left to right, respectively). The instant jet angle (blue line) is calculated from a least squares fit of the maximum velocity across the y=const. (red points). The dynamic LES results for Re=4700 without electromagnetic forcing.

W/V_{in}), as a function of the interactive parameter ($N=B_{ref}dI/rAV_{in}^2$) for different values of Reynolds numbers, are plotted in Fig. 6. Recall that N<0 are oscillation suppressing and N>0 are oscillation enhancing modes. The vertical dashed lines indicate characteristic critical frequencies $N = \pm N_{crit}$. For a neutral case (no EMF), the jet oscillates with a constant frequency (St=0.011), which is confirmed by both LES and PIV results. When N>0, the Lorentz force brakes the incoming jet. There are no significant changes of the characteristic frequency until a critical value is reached, $N=N_{crit}$, i.e. when

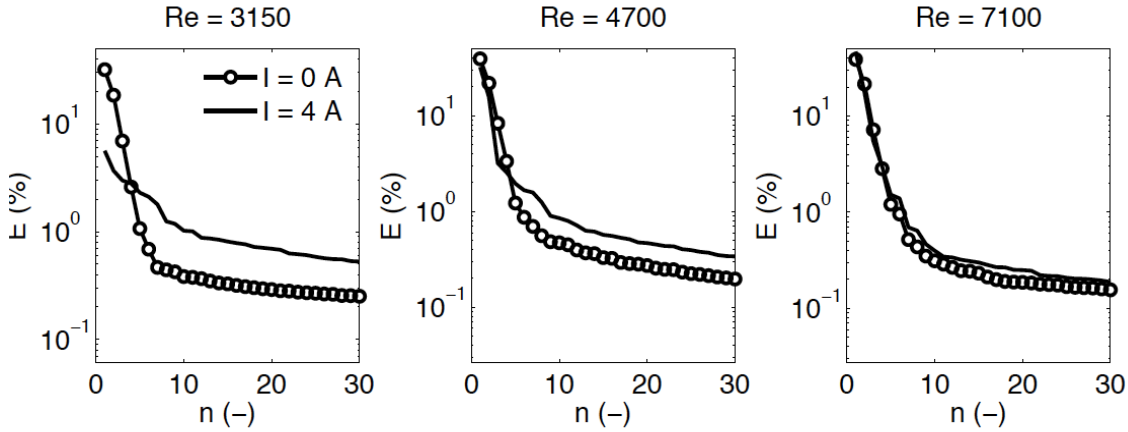

Figure 5. Distribution of the total energy contained in the velocity fluctuations (oscillatory / periodic + fluctuating / turbulence) estimated from the Proper Orthogonal Decomposition (POD) modes for neutral (I=0 A) and electromagnetically influenced (I=4 A) jets at different Reynolds numbers (Re=3150, 4700 and 7100). The velocity field is obtained from the PIV measurements, Ref.[30].

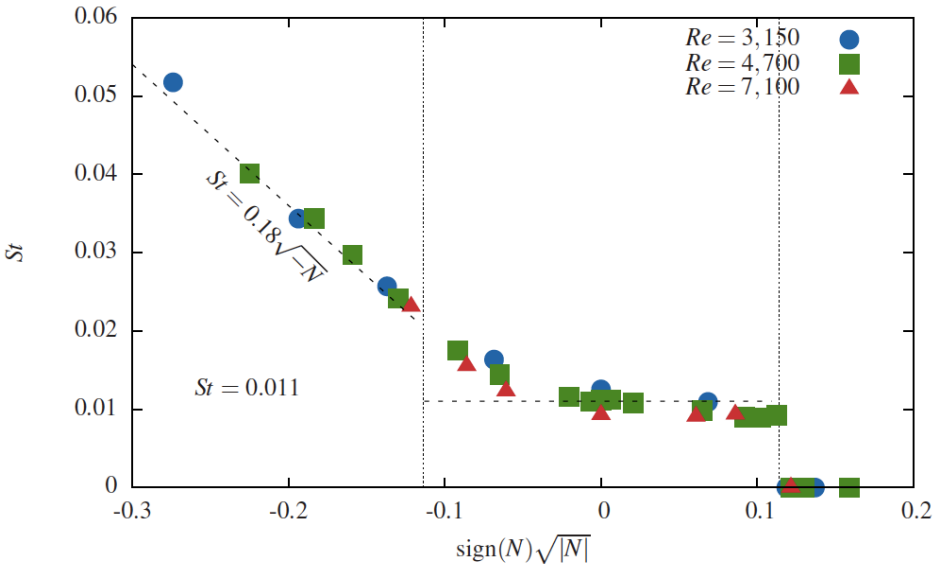

Figure 6. The characteristic frequencies (St) of the jet oscillations (Re=3150-blue circles; Re=4700-green squares; Re=7100 – red triangles) subjected to electromagnetic forcing (N) of different orientation and strength (N<0 – oscillation suppressing; N>0 – oscillation enhancing). The dashed vertical lines indicate N = $\pm N_{crit}$. Results from dynamic LES simulations.

the EMF overtakes the inertial effects. This leads to complete suppression of the jet oscillations. For N<0, the Lorentz force supports the incoming jet, leading to an increase in jet oscillations. The resulting frequency scales as $St \propto (-N)^{1/2}$ for all values of Re considered. We conclude that the EMF can significantly affect regimes of jet oscillations in a shallow confined cavity. Three characteristic regimes can be distinguished, which are separated by the characteristic critical interactive parameter N_{crit} (for the range of working parameters analyzed we find that N_{crit}=0.013): the self-oscillatory regime ($-N_{crit}<N<N_{crit}$), totally jet oscillations suppressing mode ($N>N_{crit}$) and oscillations enhanced mode

($N<-N_{crit}$). This information can be applied to different controlling strategies in practical applications where there is a necessity to locally suppress or enhance incoming jet oscillations.

4.2. Electromagnetic heat transfer enhancement in turbulent thermal convection

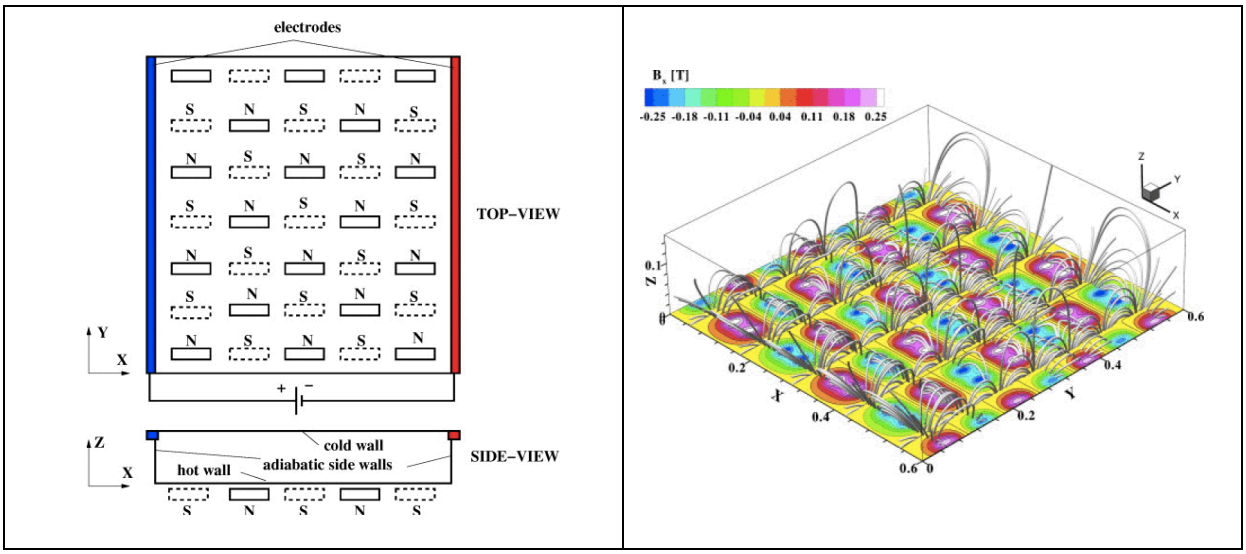

Figure 7. Left- sketch of the setup with imposed dc current through electrodes [red (right) and blue (left) sides] and permanent magnets of opposite polarities (N-S). The dimensions of the enclosure (tank) are 0.6x0.6x0.155 m^3, whereas the permanent magnets have a size of 0.084x0.04x0.04 m^3 with a magnetic strength of $|b_0|$=1 T at the surface; Right- the magnetic flux lines (gray tubes) and contours of the horizontal magnetic field component (B_x in [T]) at the bottom plate, Ref.[12].

This example deals with the combined effects of a coupled flow and heat transfer (natural convection) subjected to the external EMF. Here we explore the possibilities of producing a localized Lorentz force (constant in time) that can generate various vortical flow patterns in weakly conductive fluids leading to modification of the local wall-heat transfer, [8-10], [12]. These multiple vortical flow patterns are generated in a similar way to the previous example of the self-sustained jets, i.e. by combining arrays of permanent magnets and electrodes with supplied dc current. In contrast to the previous example (isothermal forced convection), here we mainly focus on the wall-heat transfer enhancement. We start this analysis by producing a fully developed pure thermal convection in turbulent flow regime (so called Rayleigh-Benard convection). Here, the horizontal walls are kept at constant (but different) temperatures: the bottom wall is hot and the top wall is cold, whereas all sidewalls are kept adiabatic. A moderate aspect ratio [4:4:1] enclosure is considered with a weakly conductive fluid (saltwater with σ=5.5 S/m). Beneath the lower wall an array of the permanent magnets of different polarities ((S)outh-(N)orth) is located. The electrodes of opposite polarities are placed in the upper-left and upper-right corners of the enclosure and extend along the entire length of sidewalls. A sketch of the geometry of this setup is shown in Fig.7-left. The distribution of the resulting magnetic field within the enclosure originating from an array of [5x7] permanent rectangular magnets located beneath the lower wall is depicted in Fig.7-right. The dc current from side walls is imposed on the distributed magnetic field, resulting in the Lorentz force, whose intensity can be easily adjusted by changing the strength of the supplied current. Now, various scenarios are addressed in the present research: different numbers of the magnetic dipoles (2-, 3- and 35-permanent magnets), different intensities of the imposed dc current (I=0, 1 and 10 A) and different values of the Rayleigh

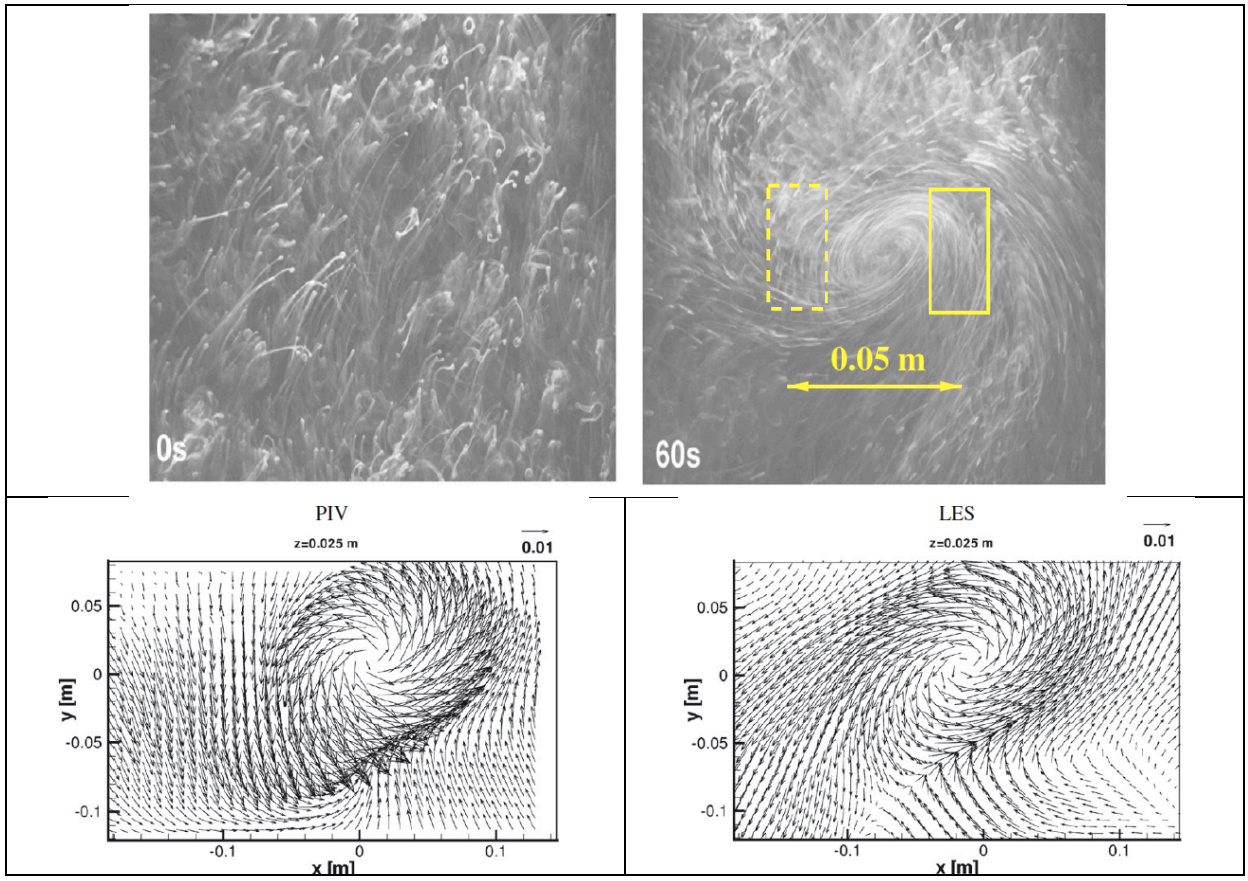

Figure 8. Top- experimental LIF visualization of the flow generated by a configuration with two-magnets beneath the tank with electrically conductive fluid and with imposed dc current of I=10 A (as shown in Fig.6) for two time instants, *t*=0 and 60 s; Bottom- the long-term averaged velocity vectors (in m/s) in a fully developed state for two-magnets configuration at z=0.025m plane, Refs. [10], [12].

numbers: Ra=10^5 - 10^9. In addition, cases with pure electromagnetic forcing (no thermal convection) are also experimentally investigated by performing LIF and PIV in characteristic vertical and horizontal planes. These datasets are used for preliminary validation of the wall-resolving LES approach. Some of the results without heating are shown in Fig.8 where the time evolutions (-top) and long-term time-averaged flow patterns (-bottom) are compared for a case with 2 magnets. This particular configuration imposes a strong planar shear in the lower part of the enclosure, which in turn generates a distinct swirling (a tornado-like) flow pattern. From Fig.8, it can be seen that LES results are in good agreement with LIF and PIV measurements (more details about comparisons between simulations and experiments are presented in [10]. After obtaining a fully developed flow and heat transfer regimes for this neutral case (pure natural convection) over a range of Ra numbers, electromagnetic forcing is initiated. The vertical profiles of the long-term time and horizontally averaged temperature for different values of Ra (10^6-10^9) and imposed dc currents (I=0 – 10 A) are shown in Fig.9. It can be seen that two distinct regions can be observed: boundary layers with very steep temperature gradients in proximity of the horizontal walls and central well-mixed core with practically a constant temperature. The electromagnetic forcing elevates the temperature in the core region and produces asymmetric distributions. This is due to significant thinning of the thermal

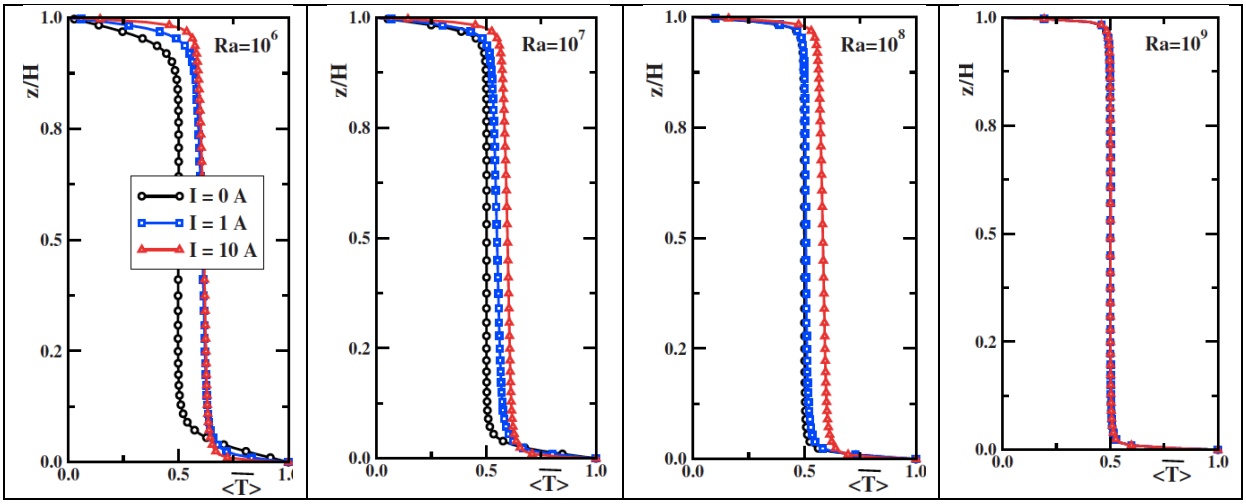

Figure 9. The long-time and horizontally averaged vertical temperature profiles for different values of Ra (10^6 – 10^9 – from left to right) and different intensities of the electromagnetic forcing I=0 (black), 1 (blue) and 10 (red) A, respectively, Ref.[12].

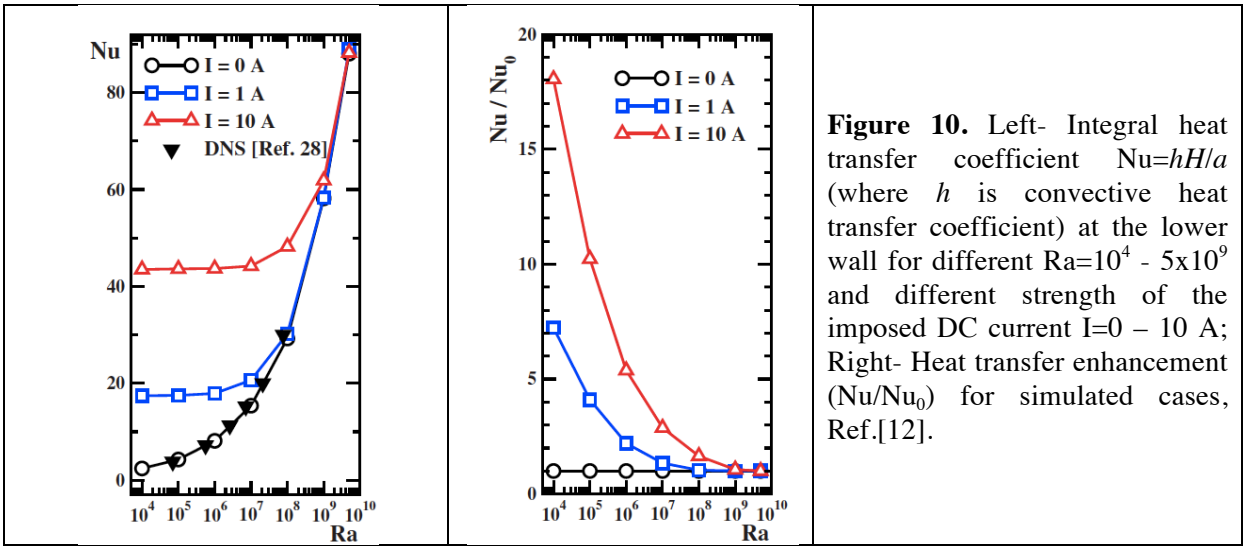

Figure 10. Left- Integral heat transfer coefficient Nu=*hH*/*a* (where *h* is convective heat transfer coefficient) at the lower wall for different Ra=10^4 - 5x10^9 and different strength of the imposed DC current I=0 – 10 A; Right- Heat transfer enhancement (Nu/Nu_0) for simulated cases, Ref.[12].

boundary layer along the lower wall compared to its neutral state at the upper wall. It can be seen that the electromagnetic effects are significant up to Ra=10^9, where almost identical distributions are obtained independent from the applied forcing. This indicates the upper limit of effective forcing since here the thermal buoyancy effects start to be the most dominant mechanism in heat transfer. The integral values (the long-term time and surface averaged) of Nusselt number are shown in Fig. 10-left. The results of the neutral case are compared with spectral DNS of [38] with much finer mesh (384^2x160) CVs. A very good agreement is obtained for the range of Ra numbers considered, providing additional credence of the wall-resolving LES approach applied here. Three regimes can be distinguished in Nu-Ra distributions: the EMF dominated regime (Ra < 10^7), the intermediate state where both the EMF and thermal buoyancy are important (10^7 < Ra < 10^9), and finally, the thermal-buoyancy-dominated regime (Ra > 10^9). To quantify these heat transfer enhancements, we plotted a

characteristic ratio of the Nusselt numbers (Nu/Nu_0) in Fig.10-right. In the EMF dominant regime a significant heat transfer is obtained in comparison with the neutral state (more than a five-fold increase). This is the consequence of an intensive mixing due to localized Lorentz force and generated vortical flow structures, which also elevate levels of the turbulent kinetic energy. The heat transfer enhancement gradually diminishes with Ra increase and the EMF effects are practically not visible at $Ra=10^9$. Finally, we conclude that application of the locally imposed EMF can be an efficient method in enhancing turbulent mixing in the turbulent thermal case. This is achieved by tailored distribution of the magnetic and electric fields, which in turn produce the Lorentz force that imposes the small vortical structures (dwarf tornados) in boundary layers as well as in the central part of the enclosure.

4.3. Flow and mixing in the wake of magnetic obstacles

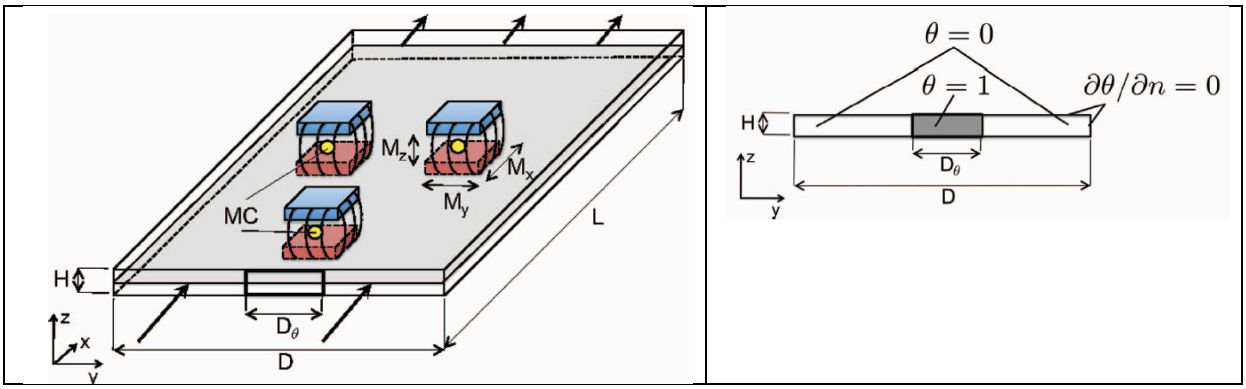

Figure 11. Left- a flow of highly conductive fluid entering a channel with adiabatic walls is considered. Sketch of the geometry with three magnetic dipoles is shown. Right- the inlet temperature and boundary conditions. Here, D_θ: D = 0.04: 0.3, Ref.[32].

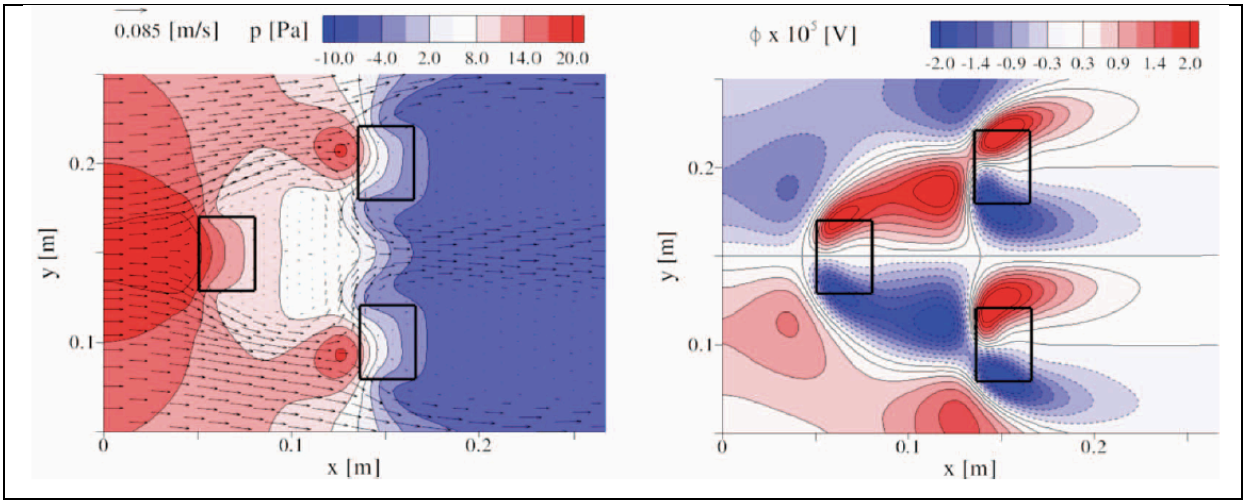

Figure 12. A zoom-in of the pressure contours and velocity vectors (-left) and of electric potential (-right) of an instantaneous flow realization in the central horizontal plane in a channel flow of a conductor subjected to localized magnetic fields, Re = 10^3, N = 10. The locations of the magnetic dipoles projections in the central horizontal plane are depicted by black rectangles, Ref.[32].

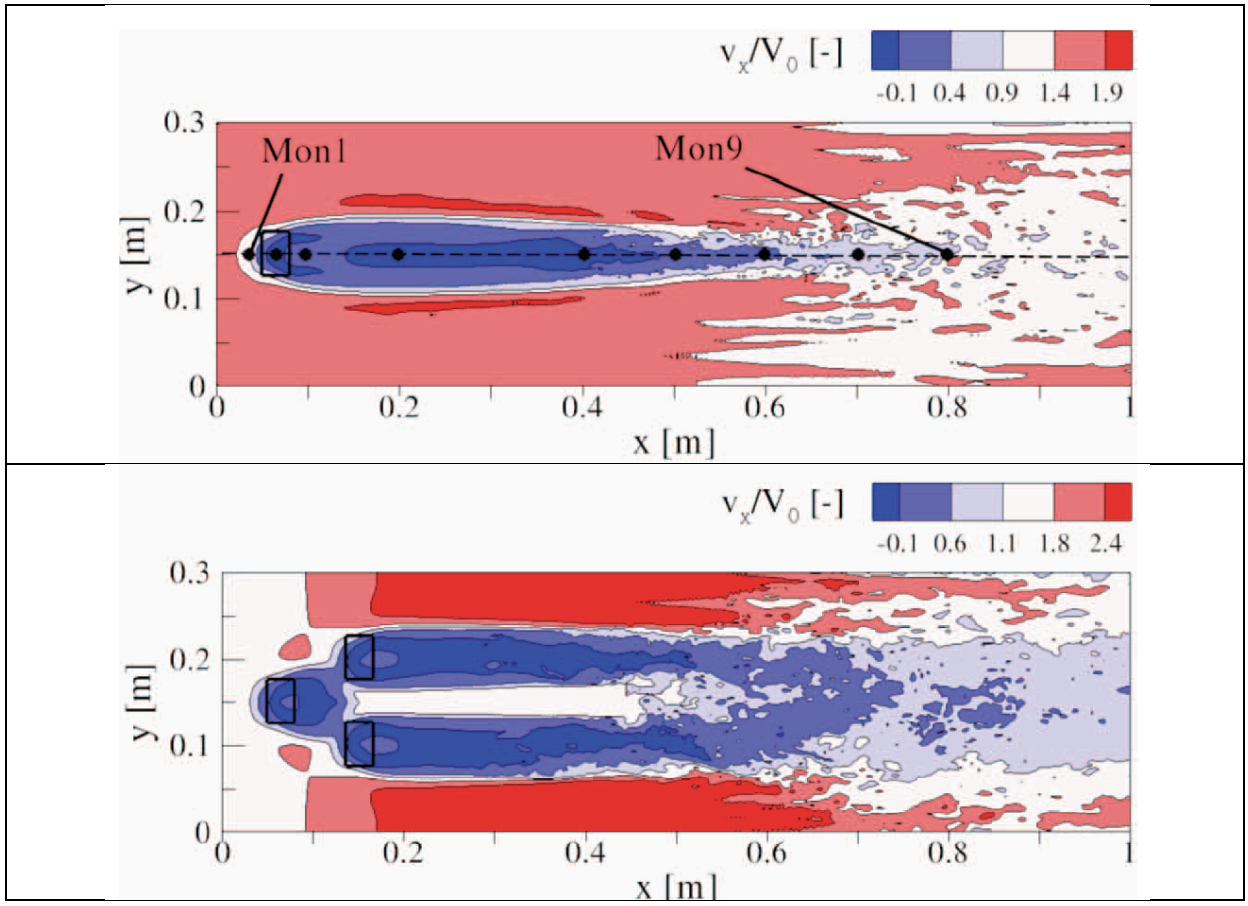

Figure 13. Contours of the instantaneous non-dimensional horizontal velocity (v_x/V_0) in the central horizontal plane for Re=1000 and N=10 for one magnetic dipole (top) and three magnetic dipoles (bottom) configurations. The locations of characteristic monitoring locations in the central horizontal plane (z = 0.01 m) along y= 0.15 m line are also shown (Mon1-Mon9) (top). The horizontal locations of monitoring points (identical for all three configurations) are: 0.0375, 0.065, 0.1, 0.2, 0.4, 0.5, 0.6, 0.7, and 0.8 m, respectively, Ref.[32].

The following example addresses a non-isothermal flow of a strongly conductive working fluid (galinstan - an eutectic alloy consisting of gallium, indium and tin, with a typical composition of 68.5% Ga, 21.5% In, and 10% Sn with typical properties: ρ = 6360 kg/m3, μ = 1.1624x10^{-3} Pa s, σ = 3.36x10^6 S/m and Pr = 0.022) entering a channel with adiabatic walls and subjected to a localised magnetic field, [31-33]. The sketch of the geometrical setup is shown in Fig.11-left. The fully developed laminar profiles are imposed at the inlet (y-z) plane (x = 0 m) with a fixed value of Re = 10^3. The inlet temperature distributions are selected to mimic the delta distribution as $\theta^* = 0$ for $0 \le y < (D/2 - D_\theta/2)$ and $(D/2 + D_\theta/2) < y \le D$, whereas $\theta^* = 1$ for $(D/2 - D_\theta/2) \le y \le (D/2 + D_\theta/2)$, Fig.11-right. Here, $\theta^* = \theta/\Delta\theta$ and $\Delta\theta = 1$. The bottom- and top-boundaries of the domain are treated as thermally and electrically insulated walls ($u = v = w = 0$, $\partial\theta/\partial n = 0$, $\partial\phi/\partial n = 0$, where "n" is the wall-normal direction). The outlet (y-z) plane is treated as a convective boundary condition for all variables, i.e. $\partial/\partial t + V_0\partial/\partial x = 0$. The side boundaries are treated as a free-slip for velocity ($\partial u/\partial n = 0$, $v = w = 0$) and a zero-gradient boundary condition is imposed for temperature and electric potential ($\partial\theta/\partial n = 0$, $\partial\phi/\partial n = 0$). We consider various configurations regarding number and orientation of the

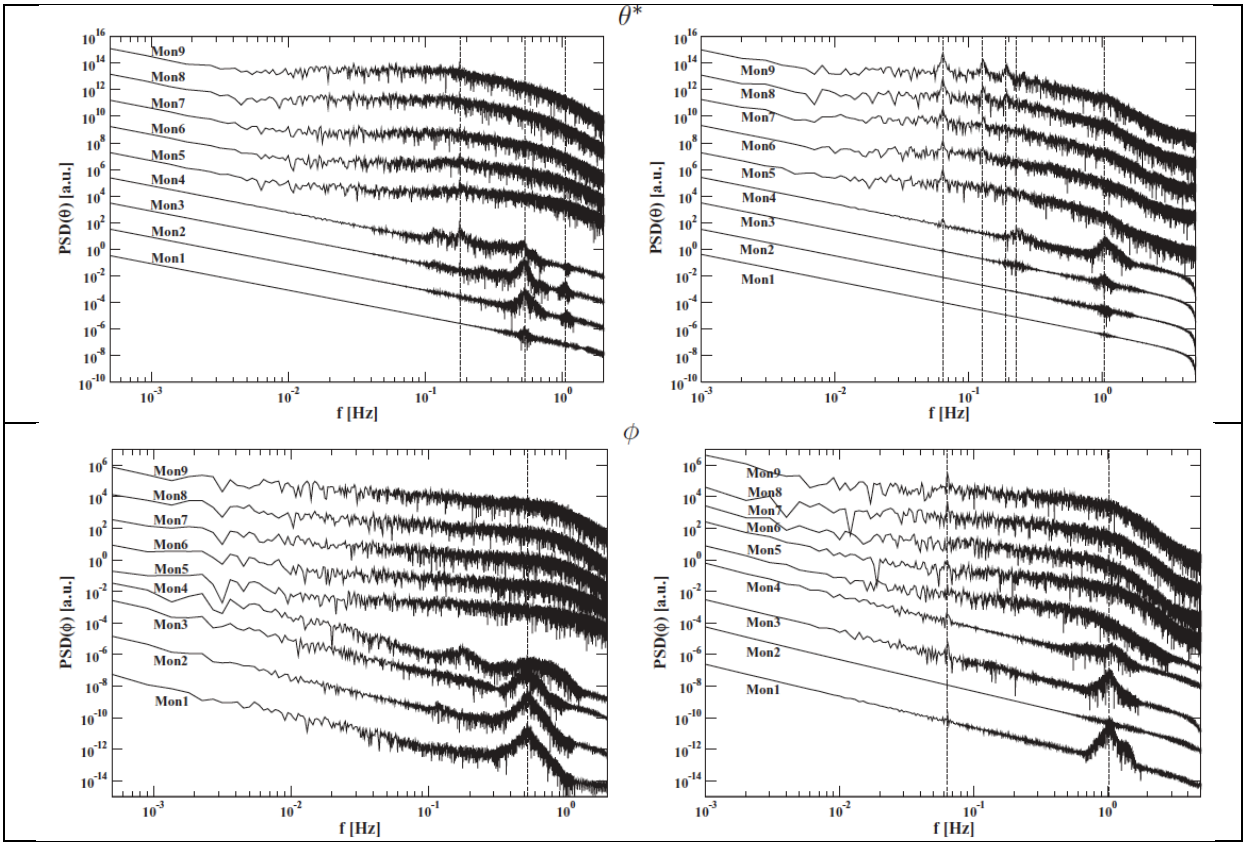

Figure 14. Temporal energy spectra of the temperature (θ*) (-top) and electric potential (ϕ) (-bottom) for 2- (-left) and 3-magnet (-right) configurations and N = 10. The graphs for Mon2-Mon9 points are shifted vertically by incrementally increasing the scaling factor by 10^2 between consecutive monitoring points. Note that dashed lines indicate the distinct key frequencies, Ref.[32].

imposed magnetic dipoles (permanent magnets). Because of the high conductivity of working fluid, here is no need to additionally impose external electric fields. Effects of the localised magnetic field are similar to flows on non-conductive fluids around the bluff bodies and are called the magnetic obstacles, [39-43]. This is illustrated in Fig.12 where a zoom-in of the pressure contours and velocity vectors (-left) and of electric potential (-right) of an instantaneous flow realization are shown for $Re=10^3$ and N=10 case with three magnetic dipoles (their locations are depicted by black rectangles). Note how the velocity vectors are partially deflected due to the Lorentz force effects from the magnetic-obstacle regions – similar to the case for the solid obstacles – but at the same time, flow reorganization within the magnetic obstacles takes place (see continuous pressure distribution within the rectangle regions). Contours of the instantaneous non-dimensional horizontal velocity (v_x/V_0) in the central horizontal plane for the one-magnetic-dipole (top) and three-magnetic-dipoles (bottom) configurations are shown in Fig.13. It can be seen that the imposed value of the interactive parameter N=10 is sufficient to produce significant braking of flow leading to generation of multiple wakes behind the magnetic obstacles. The dynamics of the instantaneous flow structures are clearly governed by the Kelvin-Helmholtz instability mechanism (presence of a strong shear). With different placement of the magnetic obstacles and with variations in their strength, numerous scenarios leading to an improved mixing can be studied in details. This is shown in Fig.14 where the temporal energy spectra of the non-dimensional temperature (θ*) and electric potential (ϕ) at different monitoring points

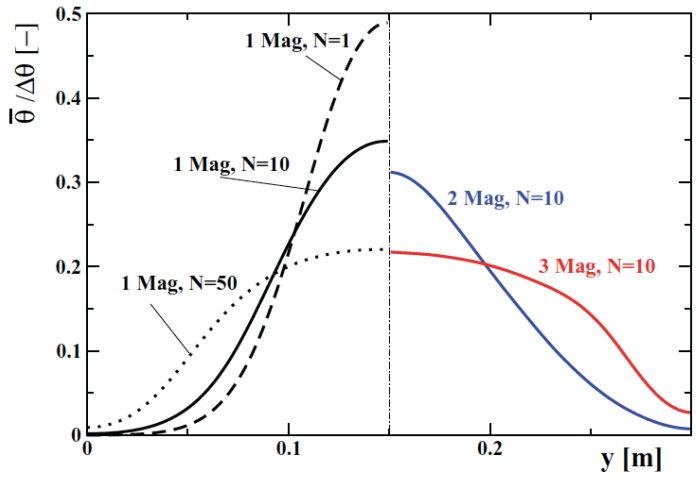

Figure 15. The profiles of the non-dimensional long-term averaged temperature (θ^*) in the central vertical plane (z/H=0.5) at the outlet of the domain (x/L = 1) for different magnetic-dipole configurations and different N, Ref.[32].

(Mon1-Mon9 – as shown in Fig.13) are plotted for 2- and 3-magnetic obstacles under identical forcing conditions, i.e. Re=10^3 and N=10. It is interesting to see that for the case of two magnetic dipoles, there is only one distinct frequency, f_1 = 0.54 Hz for the electric potential, Fig.14-bottom/left. This frequency can be observed only at Mon1-Mon6 locations. Under identical conditions, the temperature spectra shows three characteristic peaks, f_1 = 0.54 Hz, f_2 = 1.055 Hz, and f_3 = 0.177 Hz, but only at Mon1-Mon4 locations. For the three-magnetic dipoles case, two specific frequencies f_1 = 1 Hz (Mon1-Mon4) and f_2 = 0.064 Hz (Mon1-Mon9) are identified for the electric potential (ϕ), Fig.13-bottom/right. An additional three frequencies are distinguishable for the temperature, f_3 = 0.127 Hz (Mon4-Mon9), f_4 = 0.19 Hz (Mon8-Mon9) and f_5 = 0.226 Hz (Mon3-Mon4). The mixing efficiency for the configurations studied is evaluated by analyzing profiles of the long-term time-averaged non-dimensional temperature profiles in the central vertical plane (z/H=0.5) at the outlet of the domain (x/L=1), Fig.15. For a single magnetic dipole configuration, the mixing efficiency increases with increase of the interaction parameter (N), albeit in a non-linear way. In comparison with a single magnet configuration, both 2- and 3-magnet configurations produce more intensive mixing for the same value of (N). In conclusion, we show that multi-magnetic dipoles can bring additional alternation of the underlying flow of a highly conductive fluid and consequently enhanced mixing and heat transfer, when compared with a single magnet configuration. This can be utilized in practical applications where a local intensification of mixing and heat transfer is required.

4.4. Thermo-magnetic-convection of paramagnetic fluid in cubical enclosure

In the last example we report on combined experimental and numerical studies of combined natural and magnetic convection (so called thermo-magnetic convection) of a paramagnetic fluid inside a cubical enclosure heated from below and cooled from above and subjected to a magnetic field gradient. The experimental setup consists of the following components: a superconducting magnet generating a strong magnetic field, a cubical enclosure, a thermo-stating bath, a power supply and a data acquisition system, [20-22]. The superconducting helium-free magnet can generate up to 10 T of the magnetic induction, which in turn generates magnetic induction gradients up to 900 T/m2 in the magnet test section (central opening), Fig. 16-left. The central opening has a diameter of 0.1 m and length of 0.5 m. Pair of coils, which are made from the superconducting wires that must be cooled to cryogenic temperatures during operation, make the core of the magnet. The coils conduct a large electric current creating an intense magnetic field. By changing the electric current intensity through the coils, magnetic fields of different strengths can be generated. The experimental cubical enclosure

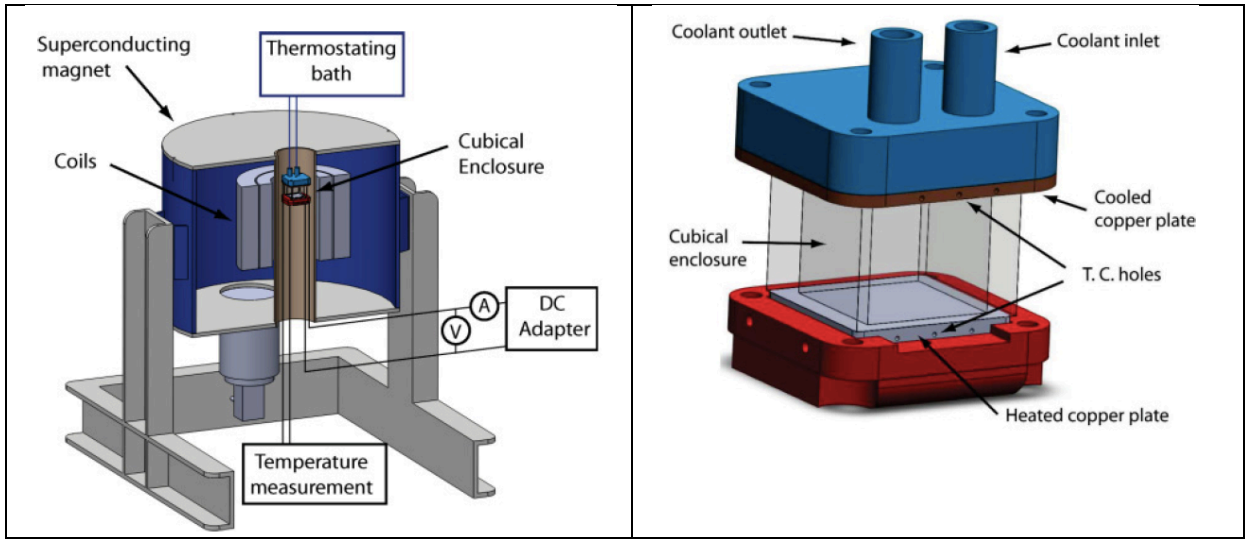

Figure 16. Left- sketch of the experimental setup and location of the cubical enclosure with paramagnetic working fluid. The superconducting helium-free magnet can generate up to 10 T in the magnet bore which has a diameter of 0.1 m and length of 0.5 m. Right- the cubical enclosure (L = D = H = 0.032 m) with copper plates and coolant inlet and outlet, Ref.[21].

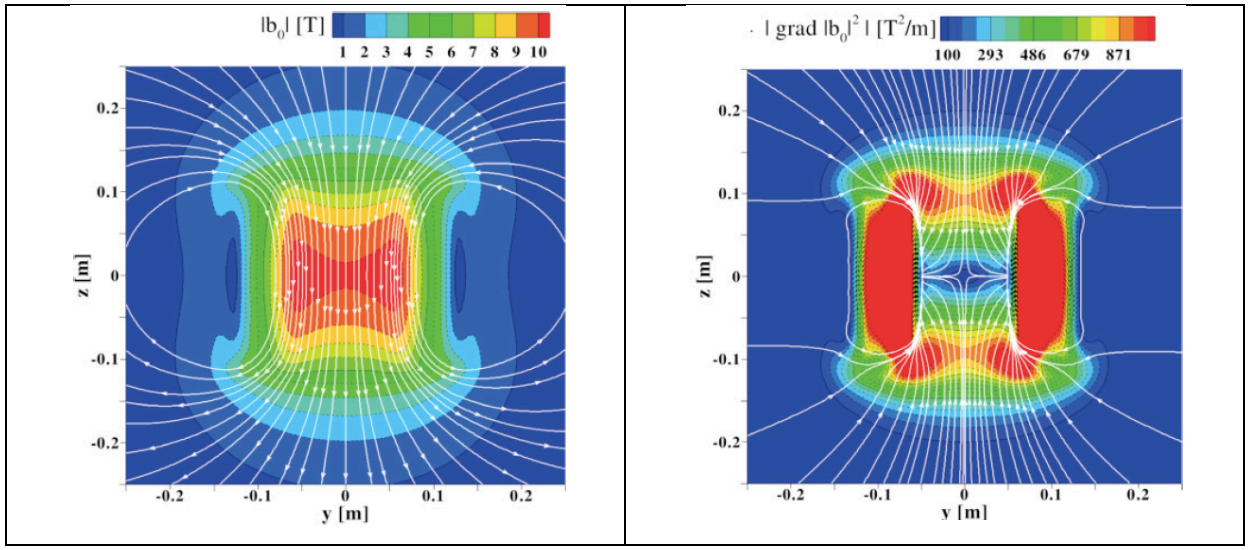

Figure 17. Calculated distributions of magnetic field (contours) and magnetic flux (lines) (-left) and of the magnitude of the magnetic square gradients (-right) in the central vertical plane (*y*-*z*) of the simulated experimental setup shown in previous figure for the upper limit of working conditions, i.e., $|b_0|_{max}$ = 10 T, Ref.[21].

(shown in Fig.16-right) could be positioned at different locations along the vertical axis of the magnet test section and can be subjected to various magnetic induction gradients. Different positioning within the magnetic test section imposes different combinations of the gravitational (thermal buoyancy) and magnetization (magnetic gradient) forces. A situation where the magnetization force enhances its gravitational counterpart can be achieved by placing the enclosure filled with a working fluid in the upper half part of the magnetic test section, i.e. at (x = 0 m, y = 0 m, z = 0.1 m), which corresponds to

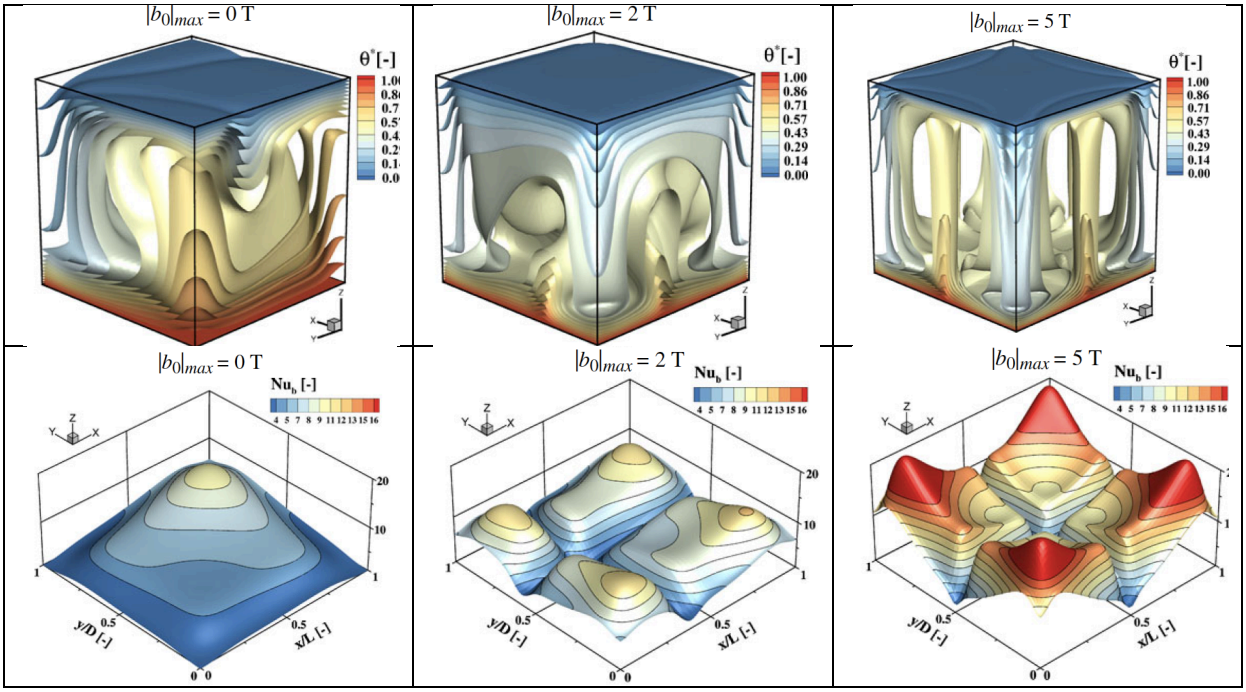

Figure 18. Top- the iso-surfaces of the temperature for different strengths of the imposed magnetic field, $|b_0|max$ = 0, 2, 5 T and a fixed value of Pr = 400. Bottom- distributions of the local Nusselt number at the lower (hot) wall. The characteristic value of thermal Rayleigh number for the neutral case is $Ra_T = 2x10^5$, Ref.[22].

the position of the upper maximum gradient of magnetic field induction ($|b_0|^2$). The details of the cubical enclosure (with L = D = H = 0.032 m) are shown in Fig. 16-right. We use paramagnetic fluids based on a 0, 50 or 80 % volume aqueous solution of glycerol with 0.8 mol/(kg of solution) concentration of gadolinium nitrate hexahydrate ($Gd(NO_3)_3*6H_2O$). The characteristic values of Prandtl numbers of working fluids are in the $10 \leq Pr \leq 584$ range. In Fig.17, we show the calculated distributions of magnetic field (contours) and magnetic flux (lines) (-left) and of the magnitude of the magnetic square gradients (-right) in the central vertical plane (y-z) of the simulated experimental setup for the upper limit of working conditions, i.e. $|b_0|_{max}$ = 10 T. An example of the influence of the imposed magnetic field induction gradient on reorganization of flow, thermal plumes and wall-heat transfer is shown in Fig. 18. The characteristic value of thermal Rayleigh number for the neutral case is $Ra_T = 2x10^5$ and different strengths of the imposed magnetic field induction are analyzed ($|b_0|max$ = 0, 2, 5 T) for a fixed value of Pr = 400. By focusing on thermal plumes, Fig.18-top, it can be seen that stronger magnetic field induction gradients produce symmetric distributions, with cold thermal plumes along the cube corners and with hot thermal plumes originating from the middle of side walls. The effects of the thermal plumes reorganization on wall-heat transfer are analyzed next, Fig.18-bottom. For the neutral case, the local Nusselt distribution shows the presence of the main diagonal symmetry with a characteristic single peak in the upper corner, Fig.18-bottom/left. Four characteristic peaks of the local Nusselt number are obtained for $|b_0|_{max}$ = 2 T case, which are symmetric with respect to the y/D=0.5 line, Fig.18-bottom/middle. Note that these peaks correspond to locations where the cold thermal plumes are hitting the lower wall. With further increase of the imposed magnetic field induction gradient, the four distinct peaks are still present, but now with a fully symmetrical distribution with respect to y/D=0.5 and x/L=0.5 lines, Fig.18-bottom/right. The time evolution of the total Nusselt number, which is calculated as a sum of overall Nusselt numbers at the hot and cold horizontal walls ($Nu_T = Nu_H + Nu_C$), is shown in Fig. 19. It can be seen that this value is zero for the

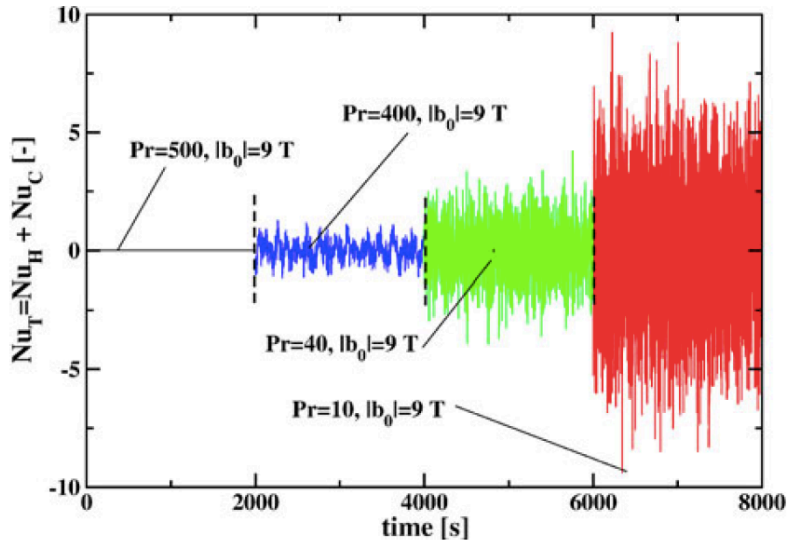

Figure 19. The time evolution of the total Nusselt number (Nu_T = Nu_H + Nu_C) for different values of Pr (Pr = 500, 400, 40, 10) and an imposed magnetic field of $|b_0|$ = 9 T, Ref.[22].

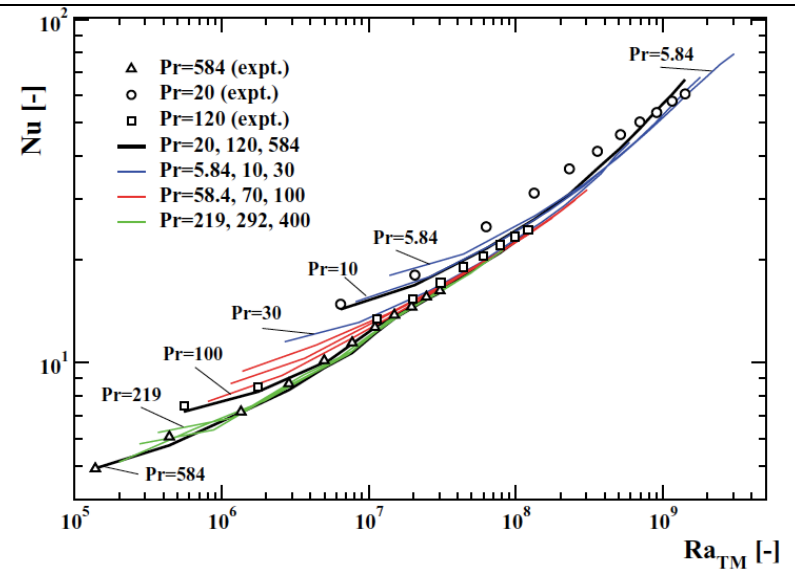

Figure 20. The Nusselt number versus the thermal-gravitational-magnetic Rayleigh number (Ra_{TM} = Ra_T + Ra_M) for the considered cases, Ref.[21].

steady laminar flow regimes (Pr = 500 and $|b_0|$ = 9 T). For lower values of Prandtl numbers (Pr = 400, 40 and 10) and for the same value of $|b_0|$ = 9 T, the total Nusselt number exhibits an intermittent behavior. A summary of all cases considered (including both experimental and numerical studies) is given in Fig.20, where the Nusselt number versus thermo-gravitational-magnetic Rayleigh number (Ra_{TM} = Ra_T + Ra_M) are shown. Three distinct regimes can be identified. The first is a transitional regime where the thermo-gravitational and thermo-magnetic mechanisms are both important, Ra_{TM} <$3x10^7$. Then, a thermo-magnetic mechanism starts to take over in the $3x10^7$ < Ra_{TM} <$3x10^8$ range. A new change in the Nusselt number slope is observed for Ra_{TM} > $3x10^8$, indicating an additional heat transfer increase. In conclusion, we have presented a detailed investigation of the flow and wall-heat transfer behavior of a paramagnetic fluid inside a differentially heated cubical enclosure subjected to strong magnetic field induction gradients over an extensive range of working parameters. Good agreement between experiments and three-dimensional time-dependent numerical simulations (DNS) in predicting integral heat transfer is obtained.

5. Conclusions and outlook

We performed combined experimental and numerical studies of the behaviour of electrically conductive and magnetized fluids in the presence of imposed electro-magnetic fields. We demonstrated that various controlling strategies could lead to significant flow reorganization, which in turn produced pre-designed levels of wall heat transfer enhancement or suppression. For weakly electrically conductive fluids, application of a proper combination of the permanent magnets and electrodes resulted in total suppression of jet oscillations. Similarly, when applied to the thermal convection case, locally generated vortical flow structures within the boundary layers, resulted in an enormous wall-heat transfer enhancement (more than a five-fold increase) over a range of Rayleigh numbers. Likewise, for the highly-electrically-conductive fluids, the mixing in the wake of magnetic obstacles can be significantly improved over a range of Reynolds and interactive numbers. Finally, the application of the strong magnetic field gradients to paramagnetic fluids confined in a differentially heated cubical enclosure, revealed that effects of the gravitational field can be entirely eliminated. This can lead to efficient flow and heat transfer optimization methods in novel crystal growth applications.

Acknowledgments

The Dutch Technology Foundation (STW), TATA Steel and ABB are acknowledged for financial support. The Marie Curie Visiting Professorships (2007-2013) and great hospitality during stays at the AGH University of Science and Technology, Krakow, Poland, are appreciated. Dr. R. Kalter and Dr. B. Righolt from TU Delft are acknowledged for experimental and numerical results of oscillating jets. Dr. E. Fornalik-Wajs, Dr. W. Wrobel and Dr. L. Pyrda from AGH Krakow are acknowledged for performing experiments with magnetized fluids. The NWO/NCF and SARA Computational and Network Services, Amsterdam, The Netherlands, provided the high performance computing facilities.

References

[1] Rudiger G and Hollerbach R, 2004 *The Magnetic Universe: Geophysical and astrophysical Dynamo Theory,* Wiley, Weinheim, Germany
[2] Molokov S, Moreau R, and Moffatt H K, 2007 *Magneto-Hydrodynamics: Historical Evolution and Trends*, Springer, Dordrecht, The Netherlands
[3] Spiegel E A, 2010 *Theor. Comput. Fluid Dyn.* 24, 77
[4] Kenjeres S and Hanjalic K, 2000 *Int. J. Heat Fluid Flow* 21(3), 329
[5] Honji H, Ohkura M, and Ikehata Y, 1997 *Exp. Fluids* 23, 141
[6] Rossi L, Thibault J P, 2002 *Journal of Turbulence* 3, N5, 1
[7] Rossi L, Vassilicos J C, and Hardalupas Y, 2006 *J. Fluid Mech.* 558, 207
[8] Kenjeres S, 2008 *Physical Review E* 78 (6) 066309
[9] Kenjeres S, 2009, *Theor. Comput. Fluid Dyn.* 23 (6) 471
[10] Kenjeres S, Verdoold J, Tummers M J, Hanjalic K and Kleijn C R, 2009 *Int. J. Heat Fluid Flow* 30, 494
[11] Rossi L, Bocquet S, Ferrari S, de la Cruz J M G and Lardeau S, 2009 *Int. J. Heat Fluid Flow* 30, 505
[12] Kenjeres S, 2011, *Physics of Fluids* 23, 015103
[13] Kenjeres S and Hanjalic K, 2004 *Int. J. Heat Fluid Flow* 25(3), 559
[14] Braithwaite D, Beaugnon E and Tournier R, 1991 *Nature* 354, 134
[15] Tagawa T, Shigemitsu R and Ozoe H, 2002 *Int. J. Heat Mass Transfer* 45(2), 267
[16] Fornalik E, Filar P, Tagawa T, Ozoe H and Szmyd J S 2005 *Exp. Thermal Fluid Sci.* 29(8), 971
[17] Ujihara A, Tagawa T, Ozoe H, *2006 Int. J. Heat Mass Transfer* 49(19–20), 3555
[18] Akamatsu M, Higano M, Ozoe H, 2007 *Numer. Heat Transf. A Appl.* 51(2), 159
[19] Bednarz T, Fornalik E, Ozoe H, Szmyd J S, Patterson J C, Lei C W, 2008 *Int. J. Therm. Sci.* 47(6), 668
[20] Wrobel W, Fornalik-Wajs E and Szmyd J S, 2010 *Int. J. Heat Fluid Flow* 31(6), 1019
[21] Kenjeres S, Pyrda L, Wrobel W, Fornalik-Wajs E and Szmyd, J S, 2012 *Phys. Rev. E* 85(4), 046312, 1
[22] Kenjeres S, Pyrda L, Fornalik-Wajs E and Szmyd J S, 2014 *Flow Turbulence Combust* 92, 371
[23] Kenjeres S and Hanjalic K, 2007 *Phys. Rev. Lett.* 98(10), 104501
[24] Kenjeres S and Hanjalic K, 2007 *New J. Phys.* 9(306), 1

[25] Kenjeres S, 2009, *Int. J. Multiscale Comp. Eng.* 7(6), 545
[26] Shimomura Y, 1991 *Phys. Fluids* 3(12), 3098
[27] Righolt B W, Kenjeres S, Kalter R, Tummers M J, Kleijn C R, 2015 *Physics of Fluids* 27 (9) 095107
[28] Kalter R, Tummers M J, S. Kenjeres S, Righolt B W, Kleijn C R, 2013 *International Journal of Heat and Fluid Flow* 44, 365
[29] Kalter R, Tummers M J, Kenjeres S, Righolt B W, Kleijn C R, 2014 *International Journal of Heat and Fluid Flow* 47, 113
[30] Kalter R, Tummers M J, Kenjeres S, Righolt B W, Kleijn C R, 2014 *Physics of Fluids* 26 (6) 065101
[31] Kenjeres S, ten Cate S and Voesenek C J, 2011 *Int. J. Heat Fluid Flow* 32(3), 510
[32] Kenjeres S, 2012 *Physics of Fluids* 24, 115111
[33] Kenjeres S, 2015 Chapter: On Turbulence Generation and Mixing in the Wake of Magnetic Obstacles: A DNS Study, *Direct and Large-Eddy Simulation IX ERCOFTAC Series Volume 20,* eds. J. Frohlich et all (Springer), pp 577-583
[34] Villermaux E, Hopfinger E, 1994 *Physica D: Nonlinear Phenomena* 72 (3), 230
[35] Maurel A, Ern P, Zielinska B J A, Wesfreid J E, 1996 *Physical Review E* 54 (4) 3643
[36] Kolsek T, Jelic N, Duhovnik J, 2007 *Applied Mathematical Modelling* 31 (10) 2355
[37] Bouchet G, Climent E, 2012 *Fluid Dynamics Research* 44 (2) 025505, 1873
[38] Verdoold J, van Reeuwijk M, Tummers M J, Jonker H J J and Hanjalic K, 2008 *Phys. Rev. E* **77**, 016303
[39] Cuevas S, Smolentsev S, and Abdou M A, 2006 *J. Fluid Mech.* 553, 227
[40] Cuevas S, Smolentsev S, and Abdou M A, 2006 *Phys. Rev. E* 74(5), 056301
[41] Votyakov E V, Kolesnikov Y, Andreev O, Zienicke E and Thess A, 2007 *Phys. Rev. Lett.* 98, 144504
[42] Votyakov E V, Zienicke E, and Kolesnikov Y B, 2008 *J. Fluid Mech.* 610, 131
[43] Votyakov E V and Kassinos S C, 2009 *Phys. Fluids* 21(9), 097102